

Performance Evaluation and Comparison of Three-Phase and Six-Phase Winding in Ultrahigh-Speed Machine for High-Power Application

Md Khurshedul Islam, Student Member, IEEE, Kazi Nishat Tasnim, Student Member, IEEE, Seungdeog Choi, Senior Member, IEEE, Sangshin Kwak, Member, IEEE, and Yang-Ki Hong

Abstract—This article investigates the influence of multiphase winding topologies in high-power ultrahigh-speed machines (HP-UHSM) of 500 kr/min. At this speed level, increasing the rotor's magnetic loading excites its critical bending resonances and leads to structural breakdown. On the other hand, increasing the stator's electric loading using the three-phase winding increases unwanted vibrations in a slotted stator and reduces the electromagnetic interaction of the stator and rotor in a slotless stator. Consequently, the maximum output power level of UHSM (500 kr/min or more) is limited to a few hundred watts only in the state-of-the-art. To over-come such a critical limitation, this article proposes a new design methodology for HP-UHSM, where the rotor's bending resonances and centrifugal stresses are restricted by limiting the maximum aspect ratio (L/D), and an optimal multiphase winding is adopted in the slotless stator to increase the power level by effective electric loading. Also, a multiphysics optimization is utilized to obtain the optimum magnetic loading and electric loading, where the bending resonance and other system limits are defined using multidisciplinary design constraints. It is observed that the multiphase winding provides an added degree of freedom to increase the power level of UHSM without exciting the rotor's bending resonances and structural breakdown. Using the proposed method, a multiphase 2 kW 500 kr/min HP-UHSM has been designed for the safety-critical AMEBA system and compared its multiphysics performance with the three-phase machine having the same volume. Finally, extensive experiments are

Manuscript received 8 February 2022; revised 1 May 2022 and 27 May 2022; accepted 11 June 2022. Date of publication 7 July 2022; date of current version 3 January 2023. This research was supported in part by the NSF CCSS-Comms Circuits & Sens System Program under Award 1905434. (Corresponding authors: Seungdeog Choi; Sangshin Kwak.)

Md Khurshedul Islam is with the Department of Electrical and Computer Engineering, Mississippi State University, Mississippi, MI 39762 USA (e-mail: mi264@msstate.edu).

Kazi Nishat Tasnim and Seungdeog Choi are with the Missis-sippi State University, Mississippi, MI 39762 USA (e-mail: kt1446@msstate.edu; seungdeog@ece.msstate.edu).

Sangshin Kwak is with the Chung-Ang University Seoul Campus, Seoul 156-756, South Korea (e-mail: sskwak@cau.ac.kr).

Yang-Ki Hong is with the Department of Electrical and Computer Engineering and MINT Center, The University of Alabama, Alabama, AL 35487 USA (e-mail: ykhong@eng.ua.edu).

Color versions of one or more figures in this article are available at https://doi.org/10.1109/TIE.2022.3187587.

Digital Object Identifier 10.1109/TIE.2022.3187587

performed on both prototypes to validate the effectiveness of the proposed method. It is shown that the multiphase HP-UHSM has no critical bending resonance below the 500 kr/min, and it has 16.3% higher output power with 1.18% higher efficiency and 28.6% lower back-EMF than the three-phase design.

Index Terms—Finite element analysis (FEA), multiphase winding, PM machine, six-phase machine, ultrahigh-speed machine.

I. INTRODUCTION

NRECENT years, ultrahigh-speed machines (UHSM) have achieved significant attention in many emerging applications such as fuel-cell air-compressors, spindles, turbochargers, robotics, and medicine [1]. One of the promising applications of UHSM is a mechanically-based antenna (AMEBA) system used for wireless communication in RF-denied environments [2]. It enables portable and bidirectional communication between the earth's surface and underground or undersea facilities such as submarines and mines by solving the coil antenna's excessive current and huge size problem. However, the main challenge in the AMEBA development is the design of its mechanical transmitter, i.e., a high-power (HP) UHSM without any critical bending frequency (CBF) below its rated speed. Also, it requires a high power-density (PD) and efficiency for portability. Note that the AMEBA system is designed to operate in the extremely low frequency-very low frequency bandwidth (0.3 to 10 kHz); hence, the UHSMs having an operating speed of \sim 500 kr/min or more are interested in this article.

In literature, the UHSMs have been designed with a rated speed of up to 1200 kr/min [3]–[7], but their power level is very limited. The first 500 kr/min permanent magnet synchronous machine (PMSM) was designed for mesoscale gas turbine application in 2005 [3]. It had a rated power of 100 W with 88.9% efficiency and ~20 kW/L PD. Another 500 kr/min 100 W PMSM has been designed in [4] using a multiphysics design algorithm. It replaces the high-cost amorphous stator core of [3] by Epcos-N87, but the efficiency drops to 82.4%. A 1000 kr/min 100 W PMSM has been presented in [5] for the turbo-compressor system using the same design process as

0278-0046 © 2022 IEEE. Personal use is permitted, but republication/redistribution requires IEEE permission. See https://www.ieee.org/publications/rights/index.html for more information.

[3]. In [6], a 500 kr/min 300 W PMSM has been designed for a rotating optical scanner application. Besides the PM machines, a switched reluctance machine of 1.2 million r/min 100 W has also been studied in [7]. However, none of these UHSMs are suitable for the AMEBA system because they are designed for low-power applications. They have either very low shaft torque at UHS or a poor PD. Thus, the maximum power level of UHSM at 500 kr/min or more is limited to 300 W only in the state-of-the-art (SOTA).

The output power of an electric machine can be improved by increasing the stator's electric loading (SEL) or the rotor's magnetic loading (RML). Unlike conventional electric machines, the RML of UHSMs is highly restricted by the excessive air-friction loss and mechanical performance, such as the centrifugal force and the CBF [6]. Hence, the only remaining option to improve the power level of UHSM is to increase the SEL. Considering the use of UHSMs in a safety-critical AMEBA system, a slotless stator is mandatory to reduce the torque ripple caused by slot harmonics. In SOTA, the stator design of UHSM is limited to the conventional three-phase winding system, where SEL is increased by using a higher input current or coil turn [3]–[7]. However, this technique presents several drawbacks in the HP-UHSM design. First, increasing input current and coil turn in a slotless stator increases the effective airgap length of the machine exponentially, which reduces the electromagnetic interaction between the stator and rotor. As a result, the machine efficiency and PD drop significantly. Second, the back-EMF of a PM machine is proportional to the rotational speed and the number of coil turn. Hence, with more coil turn, the UHSM will require a huge dc-link voltage to operate at UHS. Finally, this technique also affects the machine's thermal performance, especially it increases the PM axial temperature variation, which leads the magnet to uneven magnetization. In [6], it is attempted to improve the output power of a 500 kr/min PMSM by increasing the SEL in the three-phase winding. The output power is increased from 100 to 300 W, but the active PD drops from \sim 20–12 kW/L, the efficiency decreases from 88.9–86.1%, and the dc-link voltage increases from 15-35 V.

As a solution to this problem, a multiphase winding (more than three) can be adopted in the slotless UHSM to increase the SEL effectively. Adding more phases in UHSM will reduce the amplitude of the phase current or number of coil turn, resulting a smaller effective airgap length and lower back-EMF constant. Furthermore, it provides more room to rotor sizing which will allow to avoid any CBFs and structural breakdown below the rated speed. It will also reduce the machine vibration (due to torque ripple) by decreasing the PM axial temperature variation.

Multiphase electric machines have gained significant attention recently in electric vehicles, aircraft, naval propulsion, and high-power applications because of their inherent adventages, such as fault-tolerant capability, high torque-density, and power splitting among more phases [8]. The first multiphase (five-phase) machine was introduced in 1969 [9]. Later, extensive research has been done in developing various multiphase winding configurations up to 15 phases and their control algorithms [10]–[16]. These multiphase windings have been used to solve various problems in modern electric machines, such as

torque pulsation reduction [11], de link voltage reduction [12], efficiency improvement [13], saliency increment [14], NVH reduction [15], and PD improvement of ferrite-based machines [16]. As machine topology, multiphase windings have been studied in different rotor topologies, such as induction machines, PM machines, flux-switching machines, and reluctance machines. However, these studies on multiphase windings are limited to low-speed machines only with the conventional slotted geometry. The optimization and implementation of multiphase winding on the slotless UHSM have never been explored yet in the literature, to the best of the author's knowledge.

The main contribution of this article is the development of a new design methodology for UHSM using multiphase winding system to effectively increase its output power level without having any CBF below its rated speed. Using the proposed method, a 2 kW 500 kr/min UHSM is developed, which is the highest power level at 500 kr/min or more speed. In addition, a multiphysics performance comparison between a three-phase and six-phase HP-UHSM is presented.

The rest of this article is organized as follows. Section II presents the motivation of multiphase winding in UHSM. Section III presents the design methodology of HP-UHSM. Section IV presents the optimal design of a six-phase and three-phase HP-UHSM. The multiphysics performance comparison using FEA and experiment is presented in Sections V and VI. Finally, Section VII concludes this article.

II. EFFECTIVE ELECTRIC LOADING INCREASE IN SLOTLESS STATOR USING MULTIPHASE WINDING

According to [17], the output power of a PM machine is directly depended on the stator's electric loading (A_{stator}) and rotor's magnetic loading (B_{rotor}) as

$$P_{\text{out, PM}} = A_{\text{stator}} \times B_{\text{rotor}}.$$
 (1)

UHSMs use a slotless stator to eliminate slot harmonics. The electric loading of a slotless PM machine is defined as [17]

$$A_{\text{stator}} = \frac{2 m I_a N_{TP}}{\pi D_q} \tag{2}$$

where m is the number of phases, I_a is the per phase input current, N_{TP} is the number of turns-per-phase, and D_g is the average airgap diameter. In [3]–[7], all UHSMs use a three-phase winding and increase the SEL using a higher I_a and N_{TP} . However, this technique is not suitable for increasing the SEL effectively in the slotless UHSM due to following reasons.

First, UHSMs use multistrand Litz coil instead of single conductor to reduce the coil eddy current loss at high-frequency operation. However, when the I_a is increased to improve the SEL, the required parallel strand (N_{PS}) of Litz coil increases exponentially to safely withstand the input current. For 40-AWG coil, the required N_{PS} for a given I_a is derived as (3) from Fig. 1

$$N_{PS} = 0.4 I_a^2 + 8.6 I_a + 3.4.$$
 (3)

Fig. 1 also shows that increasing N_{PS} increases the nominal diameter (d_s) of the Litz coil considerably. For example, when N_{PS} is increased from 42 to 125 turns, d_s is increased from 0.7–1.4 mm. Such an increment in coil diameter will significantly

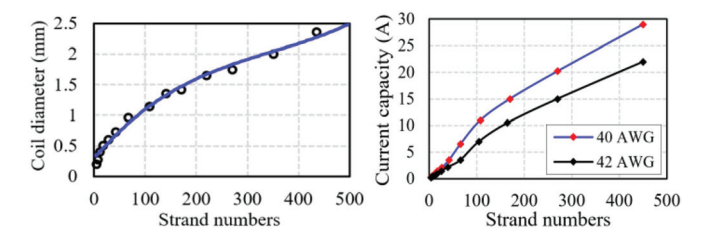


Fig. 1. Coil diameter (unserved) and peak current carrying capacity vs strand numbers of Litz coil, obtained by using manufacturer data [18].

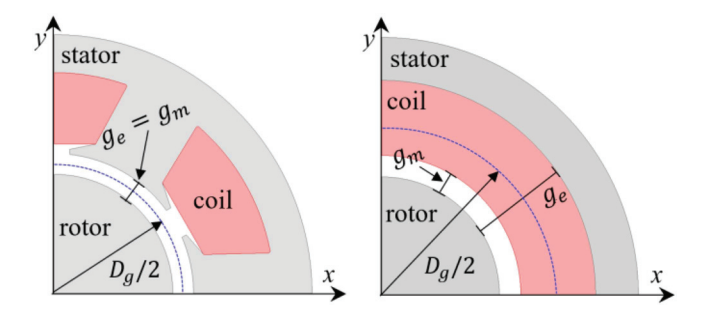


Fig. 2. Effective airgap length difference in slotted and slotless stator.

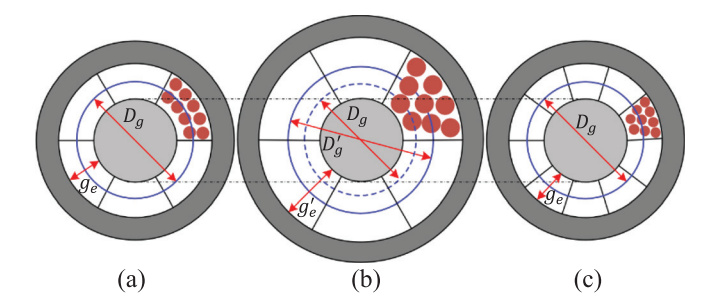


Fig. 3. Effective airgap length and average airgap diameter in the slotless stator.

increase the required-slot-area and end winding length of the phase winding. The slot area of the Litz coil is calculated as [18]

Slotarea
$$(S_A) = \frac{\pi d_s^2 N_{TP}}{4k_{SF}} + A_{ins}$$
 (4)

where k_{SF} is the slot fill factor, and A_{ins} is the area of insulating material. Increasing both the slot-area and end-winding length will drastically drop the PD of the machine, which is calculated by PD = $P_{\rm shaft}$ / $\pi R_5^2 L_e$, where L_e is the effective motor length considering end-winding and R_5 is the outer stator radius.

Second, the effective airgap length in the slotless stator changes with the SEL. Fig. 2 shows the slotted and slotless stator of a typical UHSM, where D_g is the average airgap diameter, g_m and g_e are the physical and effective airgap length, respectively. In slotted stator, $g_e = g_m$ and both the g_e and D_g remain constant for any change of SEL. However, in slotless stator, $g_e \neq g_m$ and both the g_e and D_g change considerably as the SEL varies. Fig. 3(a) and (b) shows that when the SEL in a slotless stator is increased by using a higher I_a , the required slot area is increased due to the larger coil diameter. As a result, both the effective airgap length and the average airgap diameter are

TABLE I IMPACT OF INPUT CURRENT ON HP-UHSM, ($N_{\mathrm{TP}}=20$)

Phase current	Output Power	Power density	Back-EMF	Efficiency
(I _{rms})	(W)	(kW/L)	(V _{peak})	(%)
3	1170	36	185	92.3
4	1387	32	166	91.9
5	1544	29	152	91.6
6	1727	26	141	91.2
7	1937	24	133	90.7
8	2090	22	126	90.1

Phase current (I _{rms})	Output Power (W)	Power density (kW/L)	Back-EMF (V _{peak})	Efficiency (%)
20	1012	38	120	91.3
30	1308	32	155	91.0
40	1575	27	185	90.7
50	1806	24	213	90.2
60	2020	21	238	89.3

increased from g_e to g'_e and D_g to D'_g , respectively. The airgap length has opposite impact on the output torque development and the average airgap diameter is inversely proportional to the electric loading as shown in (2). Both of these phenomena will reduce the electromagnetic interaction between the stator core and rotor's PM, resulting in a significant drop in the machine efficiency and torque density. A similar impact will occur when the SEL is increased using a higher N_{TP} in the slotless stator. Tables I and II present the performance variation of a slotless UHSM when the SEL is increased by applying higher I_a and N_{TP} The simulations are performed at 500 kr/min and the machine has a geometry similar to Fig. 5 with a three-phase Litz winding. The parametric analysis shows that when the I_a is increased from 3–8 A ($N_{TP} = 20$), the output power increases from 1170-2090 W. However, the PD and efficiency of the UHSM are decreased by 39% and 2.4%, respectively. Similarly, when the N_{TP} is increased from 20 to 60 ($I_a = 4 A$), the output power reaches 2 kW, but the PD drops from 38–21 kW/L and the efficiency decreases from 91.3-89.3%. Moreover, the back-EMF increases rapidly as the N_{TP} increases. It is also observed that the output power does not increase linearly with the I_a and N_{TP} . Rather, the increment becomes smaller as I_a and N_{TP} increase. Thus, increasing the SEL in a slotless UHSM by using a higher I_a and N_{TP} in the three-phase winding is not effective, because it reduces the machine efficiency and PD significantly.

To solve this critical limitation of UHSM, this article proposes to adopt a multiphase winding in the slotless stator to effectively increase its SEL. If E and I are the phase voltage and current, the input power of a multiphase motor can be written as [9]

$$P_{in} = \sum_{i=1}^{m} E_i I_i . (5)$$

From (5), it is evident that for a required input power, increasing the phase number allows to reduce the amplitude of the input current (I_a) or phase voltage (proportional to N_{TP}). Such a power splitting feature provides an additional degree of freedom to improve electric machine performance with the

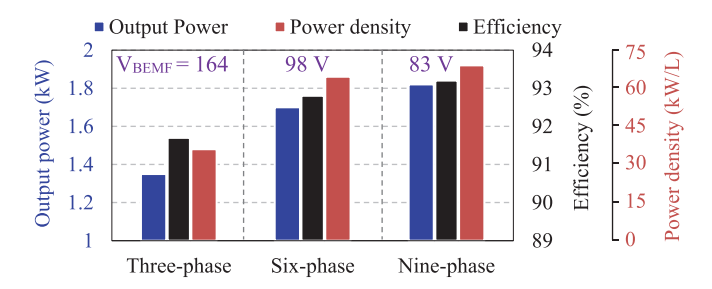


Fig. 4. Performance variation of UHSM at different winding configurations.

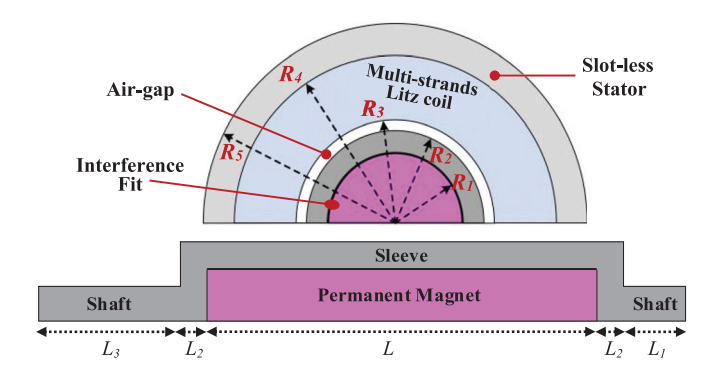


Fig. 5. 2-D geometry of the studied HP-UHSM for AMEBA application.

reduced stress on power electronic devices and reduced dc bus ripple. It also increases the slot fill factor in the machine [10]. Fig. 3(c) shows that when the SEL is increased in a slotless stator by increasing the number of phases, it reduces the I_a for the same N_{TP} , resulting in fewer N_{PS} and lower litz coil diameter, and eventually the coil requires a smaller slot area compared to Fig. 3(b). Consequently, both the g_e and D_g are smaller than 3(b) and the same as Fig. 3(a) despite having a higher SEL.

Fig. 4 shows the performance variation of a slotless UHSM when the SEL is increased by using a higher number of phases. All machines have similar geometry to Fig. 5, the same rotor and stator dimensions, and a rated speed of 500 kr/min. The simulation result shows that the three-phase design can generate a maximum output power of 1350 W at 91.6% efficiency with the specified active volume. However, the output power is increased to 1695 W in the six-phase design and 1835 W in the nine-phase design with the same volume. It is observed that as the phase number increases, the machine efficiency and PD are also increased significantly with the reduced back-EMF at UHS. Therefore, it is concluded that the multiphase winding technique can effectively increase the electric loading in a slotless stator with a higher PD and efficiency, enabling the possibility of designing the compact HP-UHSM.

III. DESIGN METHODOLOGY OF HP-UHSM USING MULTIPHASE WINDING

A systematic design approach is presented in this section to develop a robust and efficient HP-UHSM without any CBF below rated speed. First, an appropriate machine topology is selected for robust HP-UHSM. Second, the maximum possible RML limits (L&D) are determined using feasibility analysis. Third, the optimal multiphase winding topology is selected considering its effectiveness. Finally, a multiphysics optimization is performed to obtain the optimal machine geometry and winding parameters. These steps are discussed in detail as follows.

A. Machine Topology

The UHSM over 100 kr/min typically requires a simple and robust geometry to sustain at the UHS rotation [3]. Fig. 5 shows the geometry of the proposed HP-UHSM for the AMEBA system. The rotor has a cylindrical PM buried inside a retaining sleeve using the interference-fitting. Unlike a conventional rotor, the center shaft and lamination have been removed to increase its torque density. The Sm_2Co_{17} is selected for PM, considering its excellent thermal and electromagnetic characteristics. For sleeve, grade-V titanium alloy is used, which has strong mechanical properties. It also has a similar thermal expansion coefficient as Sm_2Co_{17} , which ensures a relatively constant interference fit at the high-operating temperature. A slotless stator is used to ensure a smooth torque profile. The multistrand magnetic Litz wire is utilized for stator winding to reduce the high-frequency eddy current loss of the coil. The amorphous material (Metglas) is considered for the stator core to reduce the high-frequency core loss. Different winding configurations are possible for a slotless stator, such as trapezoid self-supporting winding [19], skewed cup-shape faulhaber winding [3], and toroidal winding [4]. The winding of [3] and [19] has very low end-winding but their winding factor is ~ 0.5 . On the other hand, the toroidal winding has high winding factor with low end winding in the axial direction, but it has end-winding on the stator outer side.

B. Magnetic Loading Limit

In the studied machine geometry, the magnetic loading depends on PM usage in the rotor, mainly the rotor parameters: PM radius (R_1) and axial length (L). At 500 kr/min rated speed, both parameters are strictly restricted by the rotor's mechanical performance [6]. Figs. 6–8 show the influence of these parameters on rotor performance. These performances are analyzed using FEA and analytical model and all simulations are performed at 500 kr/min [4], [5]. PM is the most fragile material in this rotor. Rare-earth PMs are strong in compression but extremely brittle in tension. Fig. 6 shows that the tensile stress on PM increases exponentially as R_1 increases, and reaches its maximum ultimate tensile strength (UTS) limit (120 MPa) when R_1 is only 4.35 mm. At this point, the maximum tensile stress on the sleeve is 750 MPa, which is lower than the titanium's UTS limit (900 MPa). Hence, further increase of PM radius is possible by applying a high static interference-fit at the contact zone of sleeve and PM. It restricts the PM stress, but increases the sleeve tensile stress aggressively. It is shown that the sleeve stress reaches its maximum limit of 900 MPa at $R_1 = 4.6$ mm with a static-interference fit length of 30 μ m. In practice, achieving a 30 μ m interference-fit in such a small Sm_2Co_{17} is difficult due to the high risk of demagnetization and structural failure. Extending the sleeve

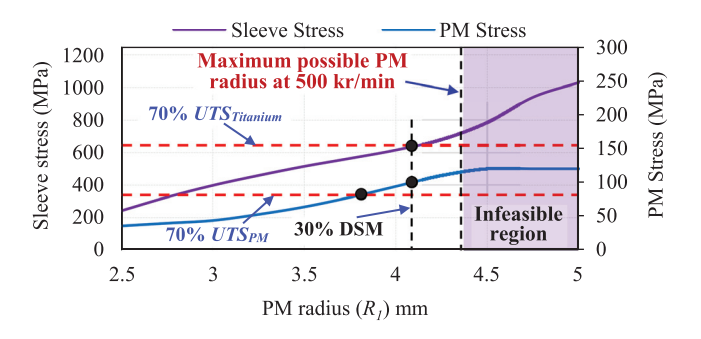


Fig. 6. Rotor stress variation versus PM radius at 500 kr/min.

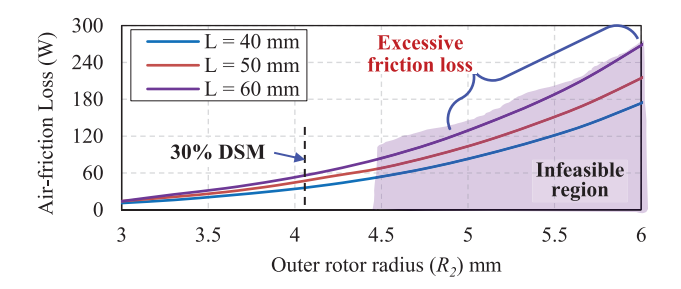


Fig. 7. Rotor air-friction loss versus rotor parameters at 500 kr/min.

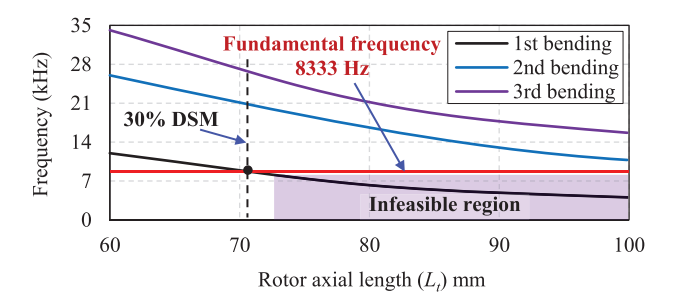


Fig. 8. Undamped mechanical resonances of the rotor at different axial length.

thickness (R_2 - R_1) is another technique for increasing the PM radius while controlling its stress development. But, it increases the air friction loss (P_f) on the rotor surface exponentially, as shown in Fig. 7. The air-friction loss is influenced by the rotor speed (ω) and design parameters as [3]

$$P_f \propto \omega^3 R_1^4 L_e \tag{6}$$

where L_e is the effective rotor axial length exposed to the stator winding. The air-friction loss reduces the machine efficiency and affects its thermal performance, especially increases the PM's axial temperature variation, leading to higher torque ripple.

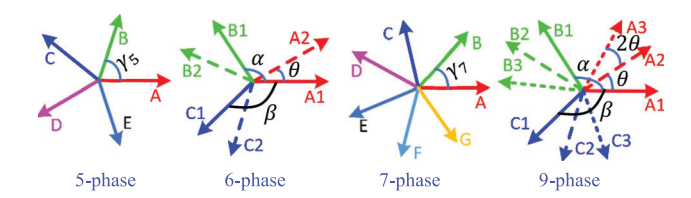


Fig. 9. Phasor diagram of different multiphase winding configurations.

On the other hand, extending the PM axial length (L) reduces the rotor's mechanical resonance frequencies below the fundamental frequency, as shown in Fig. 8. The mechanical resonances of the studied rotor can be calculated as (7) shown at the bottom of this page, where a_n is the series constant of nth resonance (w_n), E and ρ are the physical properties of rotor materials, R_1 , R_2 , L, L_1 , L_2 , and L_3 are rotor design parameters. Both the stress and bending resonance can lead the rotor to unwanted vibration, structural breakdown, and eventually a catastrophic failure at UHS operation. Hence, a good structural design safety margin (DSM) is required to ensure the safe and stable operation at UHS.

Based on these analyses, the maximum value of R_1 and L are limited to 4.15 mm and 42 mm at 500 kr/min considering a 30% DSM and the aforementioned rotor materials. Further increasing these parameters to improve the RML may cause unstable operation and mechanical failure of the UHS rotor.

C. Optimal Multiphase Winding for HP-UHSM

The phasor diagrams of the commonly used multiphase winding topologies are shown in Fig. 9 [10]-[15]. The five-phase and seven-phase configurations use an unconventional winding setup, where all phases are equally shifted by an electrical displacement angle (γ_n) . $\gamma_n = 360^o/n$, where *n* is 5 or 7. These configurations are suitable for higher fault-tolerant capability and reducing the electromagnetic force harmonic. However, the required power electronics for these configurations, such as five-phase and seven-phase inverters are not commercially available yet. Moreover, a complex control algorithm and high computational power are needed to control these machines. On the other hand, the six-phase or nine-phase configurations consist of two (A1-B1-C1 and A2-B2-C2) or three (A1-B1-C1, A2-B2-C2, and A3-B3-C3) conventional three-phase winding sets. α is the phase shift between phase A1 and B1. β is the phase shift between phase A1 and C1. For a balanced system, $\alpha = \beta = 120^{\circ}$. The three-phase winding sets are separated by a displacement angle (θ) , which can be any integer or fractional number from 0 to 360°, based on the available pole/slot numbers. These configurations can be easily driven by utilizing two or three conventional three-phase inverters. Also, they have the flexibility of the "optimal-phase-selection," for example,

$$\omega_n = \sqrt{\frac{(1/512) a_n^2 (E_{SL} + E_{PM}) R_2^4}{\left[\rho_{SL} \left\{ R_s^2 L_1^4 + R_s^2 L_3^4 + 2R_2^2 L_2^4 + (R_2 - R_1)^2 L^4 \right\} + \rho_{PM} R_1^2 L^4 \right]}}$$
(7)

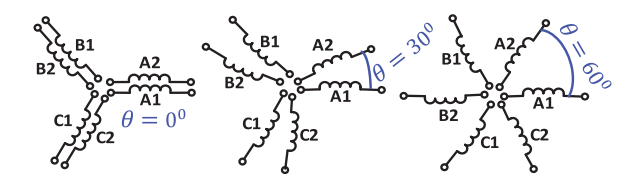


Fig. 10. Six-phase winding arrangements: (left) dual three-phase, (middle) asymmetric six-phase, and (right) symmetric six-phase winding.

a nine-phase machine can be operated as either three, six, or nine-phase based on the required power and optimal loading condition [20]. Therefore, they are more attractive over the five-phase and seven-phase configurations.

The selection between the six-phase and nine-phase depends on their effectiveness, switching losses, and installation ability for the studied system. In Fig. 4, it is observed that as the phase number increases, the output power of the studied machine is not increasing at the same rate. The increment of power level is 25.5% from three-phase to six-phase, whereas it is only 8.2% from the six-phase to nine-phase design. Because the higher slot number and more insulation materials reduce the available slot area of the nine-phase design. Moreover, increasing the phase number will also increase the switching loss, power electronics cost, and make it difficult to install in a compact UHSM. Therefore, the six-phase is considered as the optimal multiphase winding for the studied HP-UHSM.

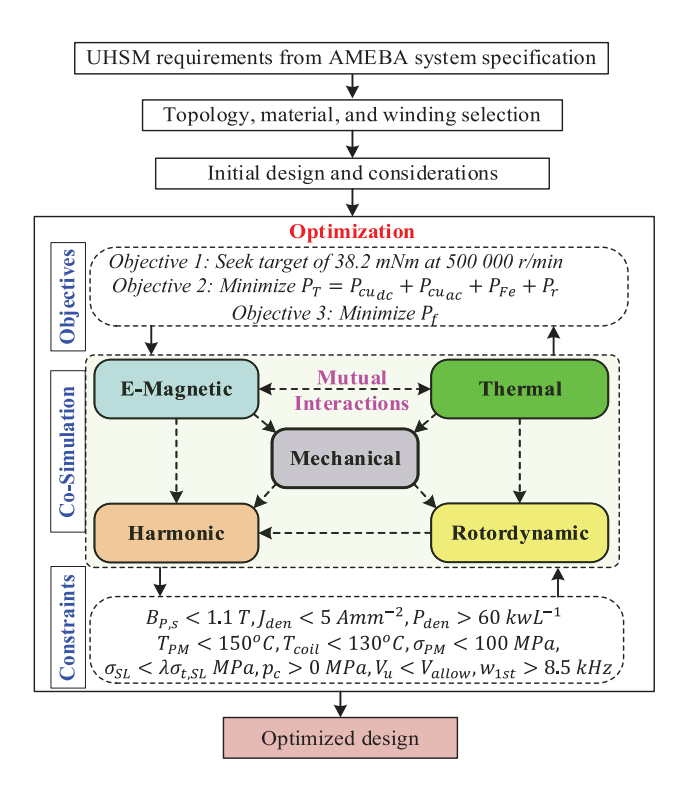
A six-phase winding can be classified into the dual three-phase, asymmetric six-phase, and symmetric six-phase arrangement based on the displacement angle (θ) between the two three-phase winding sets, as shown in Fig. 10. Among these, the asymmetric six-phase winding is the most attractive because it reduces the torque ripple by canceling the sixth torque harmonic [21]. Considering the neutral point connection, the six-phase winding has two options: single neutral point and dual neutral point. The single neutral point offers better fault-tolerant capability, but it needs extra care to control the zero-sequence current. In this article, the dual neutral point is considered, which avoids the zero-sequence current flow and has better dc bus utilization capability [22]. Considering the two-individual control model, the total electromagnetic torque of the asymmetric six-phase PMSM is derived as [13]

$$T_{\text{out}} = m \frac{p}{2} \left[(\psi_{d1} i_{q1} - \psi_{q1} i_{d1}) + (\psi_{d2} i_{q2} - \psi_{q2} i_{d2}) \right]$$
 (8)

where p is the pole number, ψ_{d1} , ψ_{q1} , i_{d1} , and i_{q1} are dq-axis flux linkages and currents of first winding set, and ψ_{d2} , ψ_{q2} , i_{d2} , and i_{q2} are dq-axis flux linkages and currents of second winding set.

D. Multiphysics Optimization of Multiphase HP-UHSM

In HP-UHSM, the RML is highly influenced by the rotor's material properties and manufacturing constraints. Moreover, changing the phase number has a significant impact on the machine geometry and thermal performance. Therefore, a multiphysics optimization is used in this design process to obtain



ig. 11. Multiphysics design process of HP-UHSM for AMEBA system.

the optimal RML and SEL. Fig. 11 shows the simplified multiphysics design process of HP-UHSMs for the AMEBA system. The machine sizing is performed by multiphysics optimization using a multiobjective algorithm. In the optimization model, different modules are integrated using the ANSYS cosimulation feature. The design of experiment technique is used to generate initial samples for each input design parameter. The samples are selected such that it covers the entire design space. The HP-UHSM for the AMEBA system presents several nonlinearities due to the mutual influence of its multiphysics performance. To address these nonlinearities, effective approximation models (response surfaces) are developed using the Kriging method. Kriging is a semiparametric interpolation method whose response function is defined as [23]

$$\mathcal{Y}(x) = f(x) + \mathcal{Z}(x) \tag{9}$$

where $\mathcal{Y}(x)$ is the response function of interest (unknown) of design parameter x, f(x) is the deterministic function (known) of x, and $\mathcal{Z}(x)$ is the error function with zero mean. When the optimization algorithm requests a new design point (DP), the integrated multiphysics modules are solved sequentially as E-magnetic, thermal, mechanical, rotordynamic, and harmonic. Each model shares its corresponding performance with other modules to consider the mutual influences of the multiphysics performance. For example, the thermal module uses the electro-magnetic losses and air-friction losses as the input heat source and sends the thermal information to other modules. Once all the DPs are solved, the Pareto-front will be obtained based on the defined constraints and objectives to select the optimal DP.

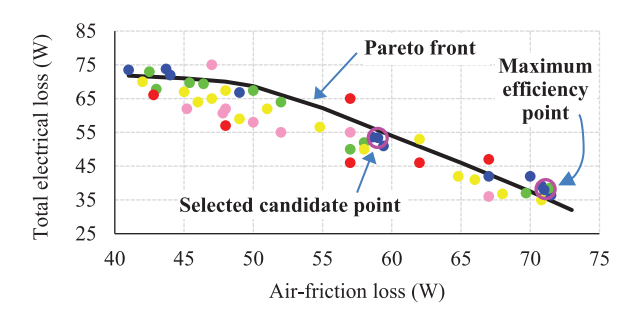


Fig. 12. Pareto-front of the six-phase HP-UHSM optimization.

IV. OPTIMAL DESIGN OF SIX-PHASE AND THREE-PHASE HP-UHSM FOR AMEBA SYSTEM

In this section, the optimal design of six-phase and threephase HP-UHSM for the AMEBA system is obtained using the multiphysics design model of Fig. 11. First, the machine specifications are derived from the targeted AMEBA system requirements, these are 38.2 mNm shaft torque at 500 kr/min, >94% efficiency, >60 kW/L PD, >30% DSM, and no CBF below the rated operating frequency. Then, the machine topology, active materials, and initial design considerations are made based on the required power/speed profile. A natural air-cooling system in the machine is considered for the portable and compact AMEBA system. Nine design variables are used including, the geometry and winding parameters. The maximum limit of R_1 and L are defined as 4.15 mm and 42 mm, which are derived in Section III-B. Several multidisciplinary design constraints associated with the AMEBA system, machine topology, materials, and manufacturing limits are considered. These include the stator peak flux density $(B_{P,S})$, maximum current density (J_{den}) , PD (P_{den}) , temperature (T_{PM}) and T_{coil} , contact pressure (P_c) , rotor stress ($\sigma_{\rm pm}$ and $\sigma_{\rm sleeve}$), vibration due to unbalanced response (V_u) , and first CBF (ω_{1st}) . The optimal DP is the one that satisfies all the specifications with constraints and provides the desired efficiency with the maximum DSM.

In this design process, first, an attempt is taken to design the targeted machine using a three-phase winding. All the multiphysics constraints are applied, such as the thermal limit, stress limit, CBF limit, and vibration limit. In this case, no feasible DP is found that satisfies the requirements, especially the output power and PD. Second, the thermo-structural and PD constraints are ignored, and the machine is optimized again using the three-phase winding. In this case, a feasible solution is obtained that satisfies the electromagnetic requirements. However, it does not meet the desired efficiency, PD, and structural DSM. It has an outer stator radius of 17.7 mm, which is beyond the limit of the AMEBA system's specification. This DP is referred to as M-1. Third, all the multidisciplinary design constraints are applied again, and the AMEBA machine is optimized using a six-phase winding configuration (30 °C displacement angle between two sets of three-phase winding). In this case, several feasible DPs are found, and the optimal DP is selected from the tradeoff between the efficiency and global DSM using a Pareto-front analysis, as shown in Fig. 12. This DP is referred to as M-2. It is observed that the DP with maximum efficiency

TABLE III
DESIGN PARAMETERS OF OPTIMIZED MACHINES

Parameters	M-1	M-2	M-3
Magnet radius, R_1 (mm)	4.1	3.9	3.9
Sleeve outer radius, R_2 (mm)	4.9	4.6	4.6
Coil inner radius, R_3 (mm)	5.5	5.2	5.2
Stator inner radius, R ₄ (mm)	15.2	11.25	11.25
Stator outer radius, R_5 (mm)	17.7	14	14
Machine Stack length, L (mm)	40	40	40
Interference-fit length, $\Delta u_o (\mu m)$	22.5	20	20
Number of turns, N_{TP}	30	20	29
Nominal coil diameter, (d _c) (mm)	1.70	1.07	1.21
Number of strands, N_{PS}	175	100	125
Input current, $I_a(A)$	6.3	3.9	4.9
Slot current density (A/mm ²)	4.41	4.84	4.71
Undamped CBF, w_{1st} (Hz)	9122	9103	9103

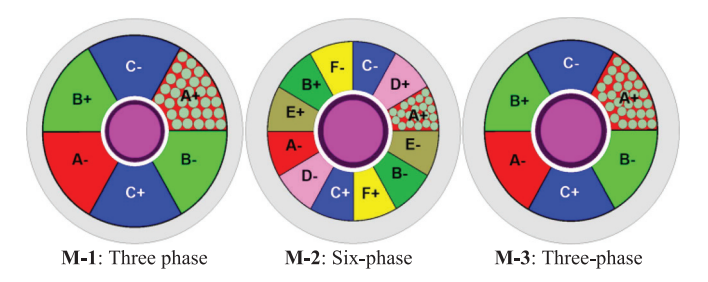


Fig. 13. Optimized HP-UHSM models for three different cases (not drawn to scale).

does not provide the required DSM, and it has only 16% DSM. Finally, to compare the benefit of the six-phase winding over the three-phase winding, the conventional three-phase winding is applied in M-2 by keeping all geometry dimensions the same. The value of N_{PS} , N_{TP} , and I_a are optimized by constraining the maximum current density as M-2. The best DP is selected and referred to as M-3. All design parameters are shown in Table III, and the machine geometries with winding pattern are shown in Fig. 13.

V. PERFORMANCE COMPARISON USING FEA SIMULATION

In this section, multiphysics performance of three optimized DPs are evaluated and compared using extensive FEA simulation. For fair comparison, all models use the same materials and the PM axial length is kept 40 mm to avoid CBF below 8.5 kHz.

A. No-Load Performance

The optimized machines are simulated at 500 kr/min with no current excitation and their line to neutral back-EMFs are shown in Fig. 14. All models have a pure sinusoidal back-EMF due to the slotless stator and cylindrical PM. The design M-2 has a peak back-EMF value of 125 V, whereas it is 160 V in M-1 and 175 V M-3. Hence, the three-phase design M-3 has 40% higher voltage stress than the six-phase design M-2. Thus, the six-phase design will require a lower dc-link at the UHS operation.

B. Full-Load Performance

All models are simulated with their optimized input, as shown in Fig. 15. Their corresponding electromagnetic torques are

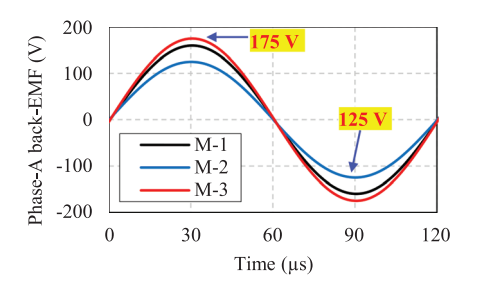


Fig. 14. No-load back-EMF at 500 kr/min.

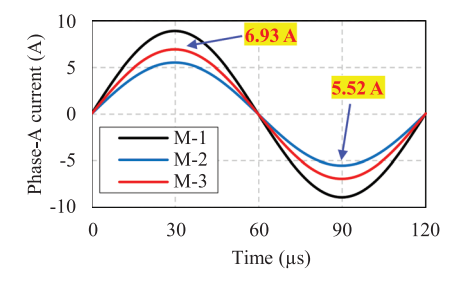


Fig. 15. Optimized input current for rated torque.

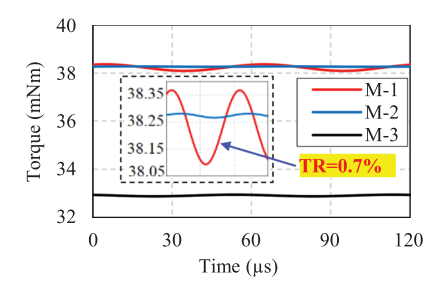


Fig. 16. Electromagnetic torque at 500 kr/min.

shown in Fig. 16 and the efficiency maps are shown in Fig. 17. The efficiency is calculated using (10), where bearing and converter

$$\eta = \frac{P_{\text{out}}}{P_{\text{out}} + P_f + P_{cu,\text{ac}} + P_{cu,\text{dc}} + P_{Fe} + P_r} \times 100\%$$
(10)

losses are excluded. The iron loss is calculated using the Bertotti iron loss separation model [24] in ANSYS Maxwell as

$$P_{\text{iron}} = P_{hy} + P_{ed} + P_{ex} = k_h f B_{p,s}^2 + k_c f^2 B_{p,s}^2 + k_e (f B_{p,s})^{3/2}$$
(11)

where $B_{p,s}$ is the peak flux-density of stator core. P_{hy} , P_{ed} , and P_{ex} are the hysteresis, eddy, and excess loss component, respectively. k_h , k_c , and k_e are the corresponding loss coefficient depend on loss data. In Maxwell, "Core loss versus frequencies" method is used to calculate these loss coefficients. The rotor's eddy current loss is calculated using the Maxwell's postprocessing capability as

$$P_{\text{rotor}} = \int_{V} \sigma E^2 dV \tag{12}$$

TABLE IV
LOSS DISTRIBUTION OF OPTIMIZED MACHINES

Parameters	M-1	M-2	M-3
Air-friction loss, P_f (W)	84	60.2	62.4
Copper dc loss, $P_{cu_{dc}}$ (W)	21.8	15.5	18.7
Copper ac loss, $P_{cu_{ac}}$ (W)	55.2	38	38.9
Rotor eddy current loss, P_r (W)	~0.2	~0.2	~0.2
Stator core loss, P_{Fe} (W)	2.2	2.2	2.1

where σ is the material conductivity, V is the effective rotor volume, and E is the electric field applied on the rotor.

It is observed that M-2 requires a sinusoidal current of 5.5 A (peak) to produce 38.2 mNm average torque (\approx 2000 W) with an efficiency of 94.5%. Whereas, M-1 requires 62% more input current to produce the same amount of torque and it has 92.5% efficiency at rated speed. Although M-3 has the same machine geometry of M-2, it produces only 32.2 mNm torque (\approx 1720 W) with 32% higher input current and 1.16% lower efficiency compared to M-2. The M-2 has a torque ripple (TR) of less than 0.1%. However, with the similar sinusoidal input current, the TR is increased to 0.7% in M-1. This is because of the PM's uneven magnetization due to its asymmetric temperature variation.

The loss distributions at the rated condition are given in Table IV. In all designs, the air-friction loss is the most dominant and it depends on R_1 . Due to lower RML requirement, the M-2 has smaller R_1 , reducing the air-friction loss by 25% than the M-1. Three-phase designs have higher ohmic loss and proximity loss due to higher dc resistance and coil volume. The total copper loss is 77 W, 53.5 W, and 57.6 W in M-1, M-2, and M-3 design, respectively. The amorphous core has very low loss coefficient, hence, the core loss is \sim 2 W for all designs. For all designs, the rotor power loss is negligible (0.2 W only) due to very small loss-coefficient of thin titanium sleeve and undistorted air-gap MMF.

The M-2 has a PD of 64.9 kW/L, which meets the AMEBA requirement. However, M-1 and M-3 have a PD of 40.6 and 55 kW/L. Thus, the six-phase winding benefits the HP-UHSM with higher efficiency, PD, and lower TR compared to three-phase.

C. Thermal Performance

The portable AMEBA transmitter has a limited cooling system for its motor drive. Hence, the thermal analysis of its HP-UHSM is important. For the studied machine, the critical thermal performances are the PM and coil temperature. The maximum PM temperature is limited by the energy product (BH)_{max} and it affects both the torque ripple, and structural performance (by thermal expansion) of the machine. On the other hand, the coil's operating temperature is crucial for the thermal insulation failure, which can lead the machine to short circuit. In this design, the maximum coil temperature is limited to 120 °C (class-F insulation) due to the natural air-cooling system. Fig. 18 shows the temperature distribution of three design models evaluated by using 3-D steady-state-thermal analysis.

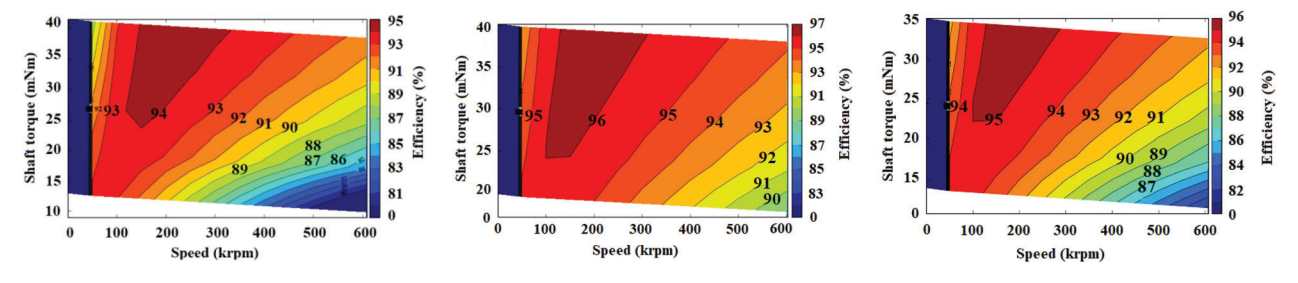


Fig. 17. Efficiency map of HP-UHSM at the rated condition: (left) M-1, (middle) M-2, and (right) M-3.

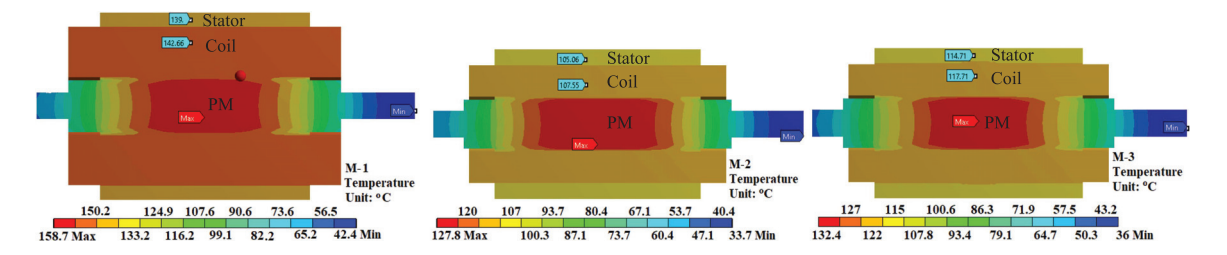


Fig. 18. Thermal analysis result of HP-UHSM at the rated condition: (Left) M-1, (Middle) M-2, and (Right) M-3).

The maximum temperature for all models is occurred in the PM due to the dominant air-friction loss on the rotor surface. At the rated operation, the maximum PM temperature is 158.7 °C in M-1, 127.8 °C in M-2, and 132.4 °C in M-3. It is clearly seen that the PM axial temperature distribution is not constant; instead, it increases from edge to center along the axial direction. Such uneven temperature distribution can cause the PM uneven magnetization, leading the rotor to unwanted torquepulsation and vibration. The PM axial temperature variation is 52 °C in M-1, 18 °C in M-2 and 38 °C in M-3. Thus, the six-phase design significantly reduces (>50%) the PM axial temperature variation compared to three-phase designs. Consequently, the M-3 has the highest TR (0.7%) and M-2 has the lowest TR (<0.1%), as shown in Fig. 16. The coil temperature is influenced by air-friction loss and electrical losses. The maximum coil temperature is 142 °C, 108 °C, and 128 °C in M-1, M-2, and M-3, respectively.

Therefore, it is concluded that the six-phase design provides a higher thermal safety than three-phase designs by reducing both the coil and PM temperature.

D. Mechanical and Rotordynamic Performance

One of the main limiting factors of HP-UHSM is the mechanical stress developed on rotor materials at the UHS rotation. Fig. 19 shows the stress distribution of M-1 and M-2 (same as M-3) rotor at 500 kr/min and rated temperature, obtained by 2-D structural FEA. The von-mises stress (VMS) yield criterion is used to predict the yielding of materials. The optimal interference fit obtained by the optimization (shown in Table III) is applied at the contact zone of the PM and sleeve.

In M-2 rotor, the sleeve experiences maximum stress of 620 MPa in its inner edge, while the maximum stress on the PM is 83 MPa in its center. Both stress values are well below their

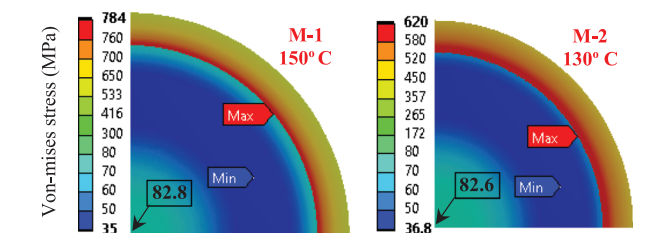


Fig. 19. VMS distribution at 500 kr/min and rated temperature.

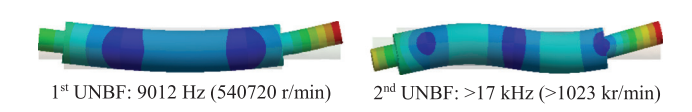


Fig. 20. Undamped natural bending frequencies of M-2 rotor using 3-D FEA.

corresponding limit. However, to maintain the same stress (83 MPa) on the PM of M-1 rotor, the sleeve experiences maximum stress of 784 MPa. The structural DSM is calculated as a ratio of the developed stress on a rotor material to the UTS limit of that material. It is found that the six-phase design M-2 has a structural DSM of \sim 31% at 500 kr/min, whereas it is only \sim 13% in the three-phase design M-1, which is 60% lower than M-2.

Finally, the rotordynamic of the six-phase rotor is studied using 3-D FEA. At the design stage, accurate calculation of CBF is highly manipulated by the rotor's guide-bearing stiffness and installation process. Hence, in this design, the rotor's undamped natural bending frequency (UNBF) is used as an indicator of the actual CBF. This consideration is rational because the actual CBF will be always higher than the UNF when the bearing damping is applied. Fig. 20 shows that the proposed six-phase UHS rotor does not have any CBF below 8333 Hz (500 kr/min).

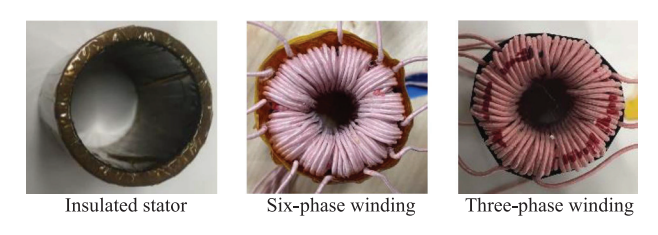


Fig. 21. Stator prototype of M-2 and M-3 machine using toroidal winding.



Fig. 22. Rotor prototype of HP-UHSM developed using shrink fit technique.

VI. PROTOTYPING AND EXPERIMENTAL VALIDATION

A. Design Comparison

The optimized six-phase (M-2) and three-phase (M-3) designs are prototyped to validate the FEA results of Section V. Fig. 21 shows the stator prototype of both machines. The slot-less stator is made by amorphous material Metglas-2605SA and insulated by a polyimide film tape. The windings for both stators are implemented in a toroidal fashion. The three-phase winding has 29 turns in a coil; hence, each phase has 58 turns in series. Each turn consists of 125 strands of 40 AWG magnet wire, forming a diameter of 1.17 mm. The six-phase winding is implemented using an asymmetric configuration as Fig. 10, where the displacement angle between two winding sets is 30°. Each coil has 20 turns, resulting 40 turns per phase in series. Each turn consists of 100 strands of 40 AWG magnet wire and has a diameter of 1.06 mm. Both coils are served using Poly-Nylon insulation (Class-F) to withstand the phase voltage. A PT100 RTD sensor is used in the winding to measuring the coil temperature. Fig. 22 shows different parts and final assembly of the UHS rotors. Both rotors have the same design geometry and materials (Sm_2Co_{17} and Titanium). They are assembled using the shrink-fit technique and have a total axial length of 72 mm. Customized ball bearings are used for UHS rotation. Fig. 23 shows the complete experimental setup, where the HP-UHSM is installed in a UHS test bench. The customized GaN-FET based inverters are used to drive the machines. A sensor-less sliding-mode speed control algorithm is developed and implemented in a digital signal processor module (TI-F28335).

B. Back-EMF Comparison

The back-EMF of both machines are measured at different speeds using cascaded motor-generator operation. Fig. 24 shows the phase-to-neutral back-EMF of phase-A for both machines at 50 kr/min. The induced voltages are sinusoidal due to cylindrical PM and slotless stator. Table V shows the back-EMF comparison between the FEA and measured results. The back-EMF constant is calculated as 2.5×10^{-4} V(r/min)⁻¹ for the six-phase and

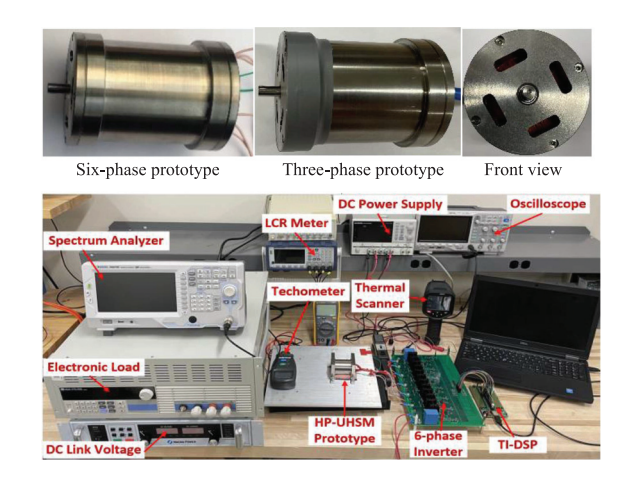


Fig. 23. Experimental setup of the HP-UHSM testing.

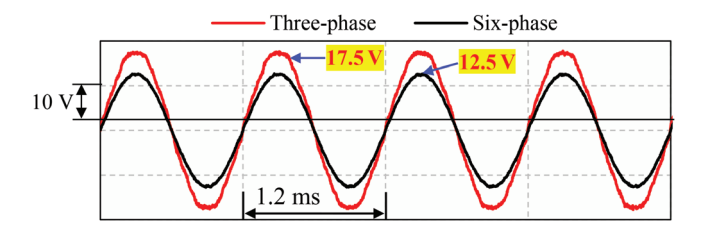


Fig. 24. Measured back-EMF of both HP-UHSMs at 50 kr/min.

TABLE V
PHASE TO NEUTRAL BACK-EMF COMPARISON

	60 kr/min		120 kr/min	
	Three-phase	Six-phase	Three-phase	Six-phase
FEA	21 V	15 V	42 V	30 V
Measured	21.4 V	15.25 V	42.5 V	30.4 V
Error	1.9%	1.7%	1.4%	1.3%

 $3.5 \times 10^{-4} \text{ V(r/min)}^{-1}$ for the three-phase machine. Therefore, the three-phase machine has 40% higher voltage stress than the six-phase machine. These values show very good agreement with the FEA results of Fig. 14 with an error of less than 2%.

C. Reaction Torque Comparison

The reaction torque is measured by connecting external variable resistors at the output terminal of the targeted machine in the cascaded motor-generator setup. The torque is calculated using $T_e=0.5mi_r\Psi_{\rm pm}$, where $\Psi_{\rm pm}$ is the PM flux linkage calculated from back-EMF analysis and i_r is the peak current through the resistor. Note that the reaction torque is measured at low speed, hence, the air friction and eddy current loss are ignored. Fig. 25 shows the testing results of both machines. The six-phase machine has a torque constant of \sim 9.82 mNm/A, and it is \sim 6.7 mNm/A for the three-phase machine. These values match with the FEA results of Fig. 16.

D. Input Current Comparison

The motoring operating of both machines are tested at different operating speeds by considering the rotor-inertia and friction-torque as the effective machine load. In this case, since

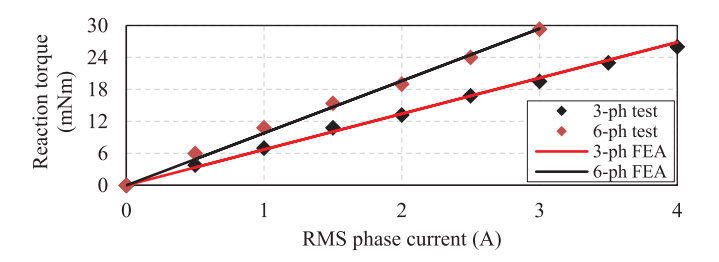


Fig. 25. Measured reaction torque of both HP-UHSMs at 50 k r/min.

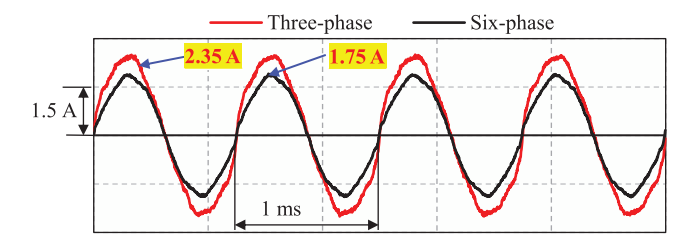


Fig. 26. Input current of both HP-UHSMs at 60 k r/min motoring operation.

TABLE VI
THERMAL PERFORMANCE (COIL TEMPERATURE)

Winding temperature of	60 k r/min (3-D FEA)	60 k r/min (Measured)	120 k r/min (3-D FEA)	120 k r/min (Measured)
Three-phase	54°C	56°C	72°C	75°C
Six-phase	50°C	53°C	66°C	68°C

both machines have the same rotor and bearing, the loading condition is also the same for both machines. Fig. 26 shows the input current (phase-A) of both machines operating at 60 kr/min (1000 Hz). It is observed that the three-phase machine draws 34% more input current compared to the six-phase machine for the same loading condition.

E. Thermal Performance Comparison

Table VI presents the comparison of thermal performance (winding temperature) between the three-phase and six-phase machine. Both machines are operated at 60 kr/min and 120 kr/min with rotor-inertia and friction-torque as operating load. The winding temperature is measured using the RTD sensor and thermal camera. The temperature is stored at 10 min interval, and it is observed that the coil temperature becomes almost steady-state after ~40 min. The testing result shows that the three-phase winding experiences higher temperature than the six-phase machine in both operating speeds. Also, the winding temperature of the three-phase machine increases rapidly when the input current (or speed) increases. The experimental result closely validates the FEA result with an acceptable error.

F. Undamped Natural Bending Frequency Test

The impulse hammer test is performed to measure the UNBF of the prototyped rotor. A tip changeable impulse hammer is used to excite the rotor mechanically, and an IEPE acceleration sensor

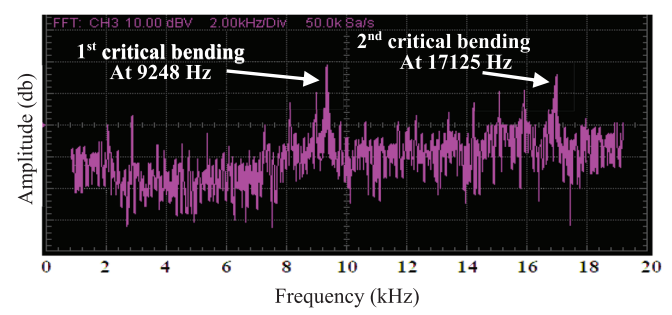


Fig. 27. Frequency spectrum result of the impulse hammer test on M-2 rotor.

TABLE VII
ELECTRICAL PARAMETERS OF BOTH MACHINES

Measured parameters	Six-phase	Three-phase
Stator phase resistance, $R_s(\Omega)$	0.17	0.25
Stator phase inductance, L_s (μ H)	69	112
Magnet flux linkage Ψ_{pm} (mVs)	2.3	3.09

is used to measure the rotor's frequency response. Fig. 27 shows the frequency spectrum of impulse test, where two sepa-rable peaks are visible in the spectrum at 9248 Hz and 17125 Hz, which are the first and second-order bending modes. The test result validates the FEA results of Fig. 20 with 1.6% error.

G. Comparison of Other Machine Parameters

Other electrical parameters are measured, as shown in Table VII. The three-phase winding has 47% higher phase resistance (dc) than the six-phase winding due to more coil turns per phase. For the same reason, the six-phase machine has a phase inductance of 69 μ H, 38% lower than the three-phase design. The PM flux-linkage of the three-phase and six-phase machine are measured as 3.09 mVs and 2.3 mVs.

For a multiphase system, the power loss in switching devices is another concern. The dominant power losses in a switching device are the conduction loss and switching loss, which can be calculated using the following simplified equation [25]:

$$P_{\text{switching loss}} = \frac{1}{2} \times V_{\text{in}} \times I_{\text{out}} \times (t_r + t_f) \times f_{\text{sw}}$$
 (13)

$$P_{\mathrm{Conduction\ loss}} = R_{DS(\mathrm{on})} \times \frac{V_{\mathrm{out}}}{V_{\mathrm{in}}} \times \left(I_{\mathrm{out}}^2 + \frac{I_{\mathrm{ripple}}^2}{12}\right)$$
 (14)

where $R_{DS(\text{on})}$, V_{in} , V_{out} , I_{out} , I_{ripple} , f_{sw} , t_r , and t_f are ON-state resistance of the switch, input voltage, output voltage, load current, ripple in the load current, switching frequency, rise time, and fall time, respectively. The total converter loss increases with the number of stitching devices. The six-phase system has twice the number of switching devices as the three-phase system. However, from (13) and (14), it is observed that at a specific switching frequency, both of these losses are a function of the dc-link voltage and square of load current, and switch resistance. In this article, the six-phase system has 28% lower dc-link voltage and 38% lower load current compared to the three-phase system. In addition, the six-phase machine has 29% lower power

conversion loss $(P_{cu} + P_{FE} + P_r + P_f)$ than the three-phase machine. Therefore, the total power loss (converter and machine losses) of the six-phase system will be comparatively lower than the three-phase system.

VII. CONCLUSION

Low-power UHSM was studied widely, and promising solution was developed for various applications. Recently, the emerging applications require both high-power and ultrahigh speed for efficient operation, such as AMEBA and fuel cell compressors. However, there are several technical challenges in increasing the power of UHSM, including 1) critical bending resonances, 2) vibration due to torque pulsation, 3) large dc-link requirement, 4) excessive rotor temperature with uneven distribution, and 5) weak electromagnetic interaction between the stator and rotor. Thus, the power rating of most UHSM was very limited (e.g., 100 W at 500 kr/min) until recently. In this article, a new design methodology using multiphase winding was proposed to design high-power UHSM for emerging applications by overcoming such technical challenges.

In addition, using the proposed method, a six-phase 2-kW 500 kr/min HP-UHSM was designed for an AMEBA system, and its multiphysics performance was compared with the threephase UHSM using the FEA and experimental testing. It was observed that the multiphase winding provides an additional degree of freedom to increase the power of UHSM by effectively improving the electric loading of slotless stators. The optimized six-phase machine has 2-kW output power with no CBF below the rated speed, 64 kW/L PD, 94.5% efficiency, 52% lower rotor axial temperature variation, and 30% DSM. The comparative analysis shows that the six-phase UHSM generates 16% higher output power with 1.18% higher efficiency, 17% higher DSM, 28.6% lower back-EMF, and negligible torque ripple than the three-phase design of the same volume. Hence, the proposed multiphase design method can be implemented to develop UHSM for other emerging applications where high output power, CBF, design safety, and portability are important factors.

REFERENCES

- G. Liu, M. Liu, Y. Zhang, H. Wang, and C. Gerada, "High-Speed permanent magnet synchronous motor iron loss calculation method considering multiphysics factors," *IEEE Trans. Ind. Electron.*, vol. 67, no. 7, pp. 5360–5368, Jul. 2020.
- [2] J. S. Glickstein, J. Liang, S. Choi, A. Madanayake, and S. Mandal, "Power-Efficient ELF wireless communications using electro-mechanical transmitters," *IEEE Access*, vol. 8, pp. 2455–2471, 2020.
- [3] C. Zwyssig, S. D. Round, and J. W. Kolar, "An ultrahigh-speed, low power electrical drive system," *IEEE Trans Ind. Electron.*, vol. 55, no. 2, pp. 577–585, Feb. 2008.
- [4] F. R. Ismagilov, N. Uzhegov, V. E. Vavilov, V. I. Bekuzin, and V. V. Ayguzina, "Multidisciplinary design of ultra-high-speed electrical machines," *IEEE Trans. Energy Convers.*, vol. 33, no. 3, pp. 1203–1212, Sep. 2018.
- [5] C. Zwyssig, J. W. Kolar, and S. D. Round, "Megaspeed drive systems: Pushing beyond 1 million r/min," *IEEE/ASME Trans. Mechatron.*, vol. 14, no. 5, pp. 564–574, Oct. 2009.
- [6] T. Baumgartner, R. M. Burkart, and J. W. Kolar, "Analysis and design of a 300-W 500 000-r/min slotless self-bearing permanent-magnet motor," *IEEE Trans. Ind. Electron.*, vol. 61, no. 8, pp. 4326–4336, Aug. 2014.

- [7] C. Gong, S. Li, and T. Habetler, "High-Strength rotor design for ultra-high speed switched reluctance machines," *IEEE Trans. Ind. Appl.*, vol. 56, no. 2, pp. 1432–1442, Mar./Apr. 2020.
- [8] E. Levi, R. Bojoi, F. Profumo, H. A. Toliyat, and S. Williamson, "Multiphase induction motor drives-a technology status review," *IET Electric Power Appl.*, vol. 1, no. 4, pp. 489–516, Jul. 2007.
- [9] E. E. Ward and H. H"arer, "Preliminary investigation of an inverter-fed 5phase induction motor," *Proc. IEE*, vol. 116, no. 6, pp. 980–984, Jun. 1969.
- [10] E. Levi, F. Barrero, and M. J. Duran, "Multiphase machines and drives-Rev-isited," *IEEE Trans. Ind. Electron.*, vol. 63, no. 1, pp. 429–432, Jan. 2016.
- [11] Q. Chen, G. Xu, G. Liu, W. Zhao, L. Liu, and Z. Lin, "Torque ripple reduction in five-phase IPM motors by lowering interactional MMF," *IEEE Trans. Ind. Electron.*, vol. 65, no. 11, pp. 8520–8531, Nov. 2018.
- [12] A. G. Yepes, J. Doval-Gandoy, and H. A. Toliyat, "Improvement in DC-Link utilization with reduced current and torque deterioration for five-phase drives by combination of circulating-current filters and simple carrier-based PWM based on closed-form expressions," *IEEE Trans Ind. Electron.*, vol. 68, no. 2, pp. 960–971, Feb. 2021.
- [13] J. Paredes, B. Prieto, M. Satrústegui, I. Elósegui, and P. González, "Improving the performance of a 1-MW induction machine by optimally shifting from a three-phase to a six-phase machine design by rearranging the coil connections," *IEEE Trans. Ind. Electron.*, vol. 68, no. 2, pp. 1035–1045, Feb. 2021.
- [14] V. I. Patel, J. Wang, D. T. Nugraha, R. Vuletić, and J. Tousen, "Enhanced availability of drivetrain through novel multiphase PM machine drive," *IEEE Trans. Ind. Electron.*, vol. 63, no. 1, pp. 469–480, Jan. 2016.
- [15] Z. Ji, S. Cheng, Y. Lv, D. Wang, W. Sun, and X. Li, "The mechanism for suppressing high-frequency vibration of multiphase surface permanent magnet motors via PWM carrier phase shifting," *IEEE Trans Power Electron.*, vol. 36, no. 9, pp. 10504–10513, Sep. 2021.
- [16] S. S. R. Bonthu, A. Arafat, and S. Choi, "Comparisons of rare-earth and rare-earth-free external rotor PMaSynRM," *IEEE Trans. Ind. Electron.*, vol. 64, no. 12, pp. 9729–9738, Dec. 2017.
- [17] J. R. Hendershot and T. J. E. Miller, Design of Brushless Permanent-Magnet Machines. Venice, FL, USA: Motor Design Books, 2010.
- [18] "New england wire technology: Litz & winding wires." Accessed: Feb. 01, 2022. [Online]. Available: https://www.newenglandwire.com
- [19] Y. Chen, J. Shen, and Z. Fang, "Topology and preliminary design of slotless brushless dc motor," in *Proc. IEEE Int. Electric Mach. Drives Conf.*, 1997, pp. WB2/7-1–WB2/7-3.
- [20] A. Cervone, M. Slunjski, E. Levi, and G. Brando, "Optimal multi-harmonic current injection strategy for an asymmetrical nine-phase PMSM," in *Proc. Int. Symp. Power Electron., Elect. Drives, Automat. Motion*, 2020, pp. 787–792.
- [21] S. Paul and K. Basu, "Overmodulation techniques of asymmetrical sixphase machine with optimum harmonic voltage injection," *IEEE Trans. Ind. Electron.*, vol. 68, no. 6, pp. 4679–4690, Jun. 2021.
- [22] Z. Liu, Y. Li, and Z. Zheng, "A review of drive techniques for multiphase machines," CES Trans. Elect. Mach. Syst., vol. 2, no. 2, pp. 243–251, Jun. 2018.
- [23] X. Sun, Z. Shi, G. Lei, Y. Guo, and J. Zhu, "Multi-Objective design optimization of an IPMSM based on multilevel strategy," *IEEE Trans. Ind. Electron.*, vol. 68, no. 1, pp. 139–148, Jan. 2021.
- [24] G. Bertotti, "General properties of power losses in soft ferromagnetic materials," *IEEE Trans. Magn.*, vol. 24, no. 1, pp. 621–630, Jan. 1988.
- [25] U. Jadli, F. Mohd-Yasin, H. A. Moghadam, P. Pande, M. Chaturvedi, and S. Dimitrijev, "A method for selection of power MOSFETs to minimize power dissipation," *Electronics*, vol. 10, 2021, Art. no. 2150.



Md Khurshedul Islam (Student Member, IEEE) received the B.S. degree in electrical and electronic engineering from the International Islamic University Chittagong (IIUC), Sonaichhari, Bangladesh, in 2014. He is currently working toward the Ph.D. degree in electrical engineering with the Mississippi State University, Starkville, MS, USA.

From 2014 to 2017, he was a Lecturer with IIUC, Bangladesh. His research interest is electric machine design and control.



Kazi Nishat Tasnim (Student Member, IEEE) received the B.S. degree in electrical and electronic engineering from the Bangladesh University of Engineering and Technology, Dhaka, Bangladesh, in 2018. She is currently working toward the Ph.D. degree in electrical engineering with the Mississippi State University, Starkville, MS, USA.

Her research interest includes control of electric machines.



Sangshin Kwak (Member, IEEE) received the Ph.D. degree in electrical engineering from Texas A&M University, College Station, TX, USA, in 2005.

From 2007 to 2010, he was an Assistant Professor with Daegu University, Gyeongsan, South Korea. Since 2010, he has been working with Chung-Ang University, Seoul, South Korea, where he is currently a Professor. His current research interests include the design, modeling, control, and analysis of power converters for electric vehicles.



Seungdeog Choi (Senior Member, IEEE) received the B.S. degree electrical and electronics engineering from Chung-Ang University, Seoul, South Korea, in 2004, the M.S. degree in electrical engineering and computer sciences from Seoul National University, Seoul, South Korea, in 2006, and the Ph.D. degree in electric power and power electronics program from Texas A&M University, College Station, TX, USA, in 2010.

He has been an Associate Professor with Mississippi State University, Starkville, MS, USA,

since 2018. His current research interests include EMI analysis, degradation modeling, motor design, and control.



Yang-Ki Hong received the B.S. degree in physics and the M.S. degree in solid-state physics (magnetism) from Yonsei University, Seoul, South Korea, in 1972 and 1974, respectively, and the Ph.D. degree in metallurgy from the University of Utah, Salt Lake City, UT, USA, in 1981

He is currently the E. A. "Larry" Drummond Endowed Chair Professor with the Department of Electrical and Computer Engineering and a Professor of materials science Ph.D. Program

with The University of Alabama, Tuscaloosa, AL, USA.